Secretory stimuli distinctly regulate insulin secretory granule maturation through structural remodeling

1 **Aneesh Deshmukh,[1] Kevin Chang,[1] Janielle Cuala,[2] Maria J. Hernandez Campos,[3] Shayan Mahmood,**
2 **Riva Verma,[4] Senta Georgia,[5] Valentina Loconte,[6,7,8] Kate L. White[*1,9]**
3 [1]Department of Chemistry, Bridge Institute, Michelson Center for Convergent Bioscience, University of Southern California,
4   Los Angeles, CA 90089, USA
5 [2]Medical Biophysics Program, Keck School of Medicine, University of Southern California, Los   Angeles, CA 90033, USA
6 [3]Department of Chemistry, Monmouth University, West Long Branch, NJ 07764, USA
7 [4]Department of Biomedical Engineering, University of Southern California, Los Angeles, CA 90089, USA
8 [5]Department of Stem Cell Biology and Regenerative Medicine, Keck School of Medicine, University of Southern California,
9   Los Angeles, CA 90033, USA
10 [6]Department of Anatomy, School of Medicine, University of California San Francisco, San Francisco, CA 94143, USA
11 [7]Molecular Biophysics and Integrated Bioimaging Division, Lawrence Berkeley National Laboratory, Berkeley, CA 94720, USA
12 [8]Present address: Diamond Light Source, Harwell Science and Innovation Campus, Didcot, Oxfordshire OX11 0DE, United Kingdom
13 [9]Lead contact
14 [*]Correspondence: katewhit@usc.edu
15

16 **SUMMARY**

17 Insulin secretory granule (ISG) maturation is a crucial aspect of insulin secretion and glucose
18 homeostasis. The regulation of this maturation remains poorly understood, especially how secretory
19 stimuli affect ISG maturity and subcellular localization. In this study, we used soft X-tomography (SXT) to
20 quantitatively map ISG morphology, density, and location in single INS-1E and mouse pancreatic β-cells
21 under the effect of various secretory stimuli. We found that the activation of glucokinase (GK), gastric
22 inhibitory polypeptide receptor (GIPR), glucagon-like peptide-1 receptor (GLP-1R), and G-protein coupled
23 receptor 40 (GPR40) promote ISG maturation. Each stimulus induces unique structural remodeling in
24 ISGs, by altering size and density, depending on the specific signaling cascades activated. These distinct
25 ISG subpopulations mobilize and redistribute in the cell altering overall cellular structural organization.
26 Our results provide insight into how current diabetes and obesity therapies impact ISG maturation and
27 may inform the development of future treatments that target maturation specifically.

28

29 **KEYWORDS**

30 Soft X-Ray Tomography, Organelle Biology, Insulin Secretory Granule, Pancreatic β-cell

31

32 **INTRODUCTION**

33 Insulin is a vital endocrine hormone responsible for regulating blood sugar levels.[1] Insulin secretory
34 granules (ISGs) are specialized organelles in pancreatic β-cells, essential for the storage, transport,
35 processing and secretion of insulin and other peptides.[2,3] Mechanistically, a major step in the lifecycle of
36 ISGs before secretion is maturation — the conversion of an immature ISG containing proinsulin into a
37 mature ISG containing active insulin for secretion. The hallmarks of ISG maturation are ISG acidification,
38 proinsulin processing to insulin via the action of processing enzymes, reduction in ISG size, and
39 condensation or crystallization of insulin to form a dense core.[4,5] Several studies have shown that people
40 with Type 1 and Type 2 diabetes (T1D and T2D respectively) often exhibit elevated levels of proinsulin
41 and low C-peptide (a byproduct of proinsulin processing), suggesting that defects in ISG maturation are
42 associated with disease.[6–9]

43 Decades of research on the fundamental cell biology of secretion have elucidated numerous cellular
44 signaling pathways that regulate insulin secretion. This has enabled the development of drugs designed

45 to increase insulin secretion for the treatment of disease.[10,11] Yet, very little information remains on the
46 cellular signals that regulate ISG maturation. Specifically, a key gap in knowledge is whether acute
47 exposure to secretory stimuli impacts ISG maturation, structural remodeling, and subcellular localization
48 of ISGs. Historically, cell function assays such as western blotting and enzyme activity assays have been
49 leveraged to study ISG maturation, leading to a thorough in-vitro biomolecular understanding of the
50 proteolytic cleavage of proinsulin to insulin.[12,13] However, these approaches often lack the sensitivity to
51 detect subtle changes at shorter timescales. Additionally, such ensemble assays lack structural and
52 spatial information, limiting our understanding of the subcellular regulation of ISG maturation within a
53 single cell.

54 Single cell structural and biophysical analysis provides a unique opportunity to understand the
55 relationship between cell structure and function.[14] To gain insights on β-cell organization, pioneering
56 studies using 3D Focused Ion Beam Scanning Electron Microscopy (3D FIB-SEM) and serial block-face
57 SEM, to map whole cells, have advanced our understanding of the distribution and spatial heterogeneity
58 of ISGs in β-cells.[15,16] However, these methods require time-intensive sample preparation, limiting high-
59 throughput screening of cellular conditions or stimuli that regulate maturation. Additionally, these
60 approaches often rely on mechanical or chemical perturbations, such as serial slicing of the sample or
61 chemical fixation, which hampers quantitative comparisons of molecular density, a key marker of ISG
62 maturity. An ideal method would allow for rapid imaging of cells in their native state with sensitive
63 detection of ISG density.

64 Soft X-Ray Tomography (SXT) is uniquely positioned as it allows us to sensitively map and measure ISG
65 maturation in pancreatic β-cells under multiple stimuli. SXT provides quantitative, near-native, high-
66 resolution (~30 nm), non-biased imaging at a single-cell level.[17–19] Using SXT, we can create whole-cell
67 3D maps of numerous β-cells, including organelles such as the cell membrane, nucleus, lipid droplets,
68 mitochondria and ISGs.[20–22] SXT allows us to identify and differentiate ISGs by their molecular density,
69 allowing us to measure a spectrum of ISG maturities. The molecular density can be quantified and
70 compared across conditions using a Linear Absorption Coefficient (LAC) value which is not possible with
71 other methods. Our previous studies employed SXT to develop whole cell maps of INS-1E cells (a rat
72 insulinoma β-cell line) and demonstrated that co-stimulation with glucose and exendin-4 (Ex-4; a
73 glucagon-like peptide receptor 1 agonist) triggers changes in insulin packing density.[18,21] This led us to
74 consider if distinct biochemical signals alter ISG maturation uniquely and enrich discrete ISG
75 subpopulations. ISGs consist of subpopulations based on factors such as pH, density, age, mobility,
76 subcellular location, protein and lipid composition.[23–36] Disease states alter ISG subpopulations[32], thus
77 understanding how secretory stimuli impact ISG heterogeneity will be beneficial for the development of
78 future therapies.

79 Given the extensive knowledge of insulin secretion signaling pathways and their widespread use in
80 treating diabetes and obesity, we leveraged these pathways to investigate whether discrete signals that
81 affect insulin secretion simultaneously influence ISG maturation. In this work, we evaluate the differential
82 effects of secretory stimuli on ISG maturation by imaging whole and fully hydrated cells using SXT. We
83 used five orthogonal stimuli: metabolic signals (High Glucose), incretins (Exendin-4 and Gastric Inhibitory
84 Polypeptide), G-Protein Coupled Receptor 40 (GPR40) agonist (TAK-875), glucokinase activator (GKA-
85 50), and a Sulfonylurea (Glimepiride). Our findings reveal that some secretory stimuli, besides enhancing
86 secretion, also increase ISG molecular density and promote ISG maturation. We show that different
87 stimuli affect the maturation process uniquely by inducing structural and biophysical remodeling of ISGs.
88 Additionally, we show that these stimuli affect overall cellular structure by mobilizing ISG pools of varying
89 maturities to discrete regions across the cell. Our approach provides new structural and spatial insights
90 into β-cell biology and reveals how secretory stimuli differentially impact ISG maturation.

91

92 **RESULTS**

93 ***SXT reveals a spectrum of ISG maturity at a single cell level.***

94 We previously demonstrated the use of SXT to map organelles in whole INS-1E cells at a 60 nm
95 resolution.[18,21] In this study, we focused on mapping ISG morphology, maturity and subcellular

96   localization achieving higher resolution tomograms using a 50-nm zone plate. This allowed us to resolve
97   individual ISGs and their sub-vesicular features (Fig 1A). INS-1E cells were imaged in 6 – 8 µm
98   microcapillaries using X-rays at the water window (284–583 eV photon energy), which provides a natural
99   contrast for carbon- and nitrogen-rich organelles. We reconstructed the projection images into 3D
100   tomograms[37] and performed semi-automated segmentation to obtain organelle masks of the nucleus,
101   ISGs, mitochondria and cell membrane. This enabled the generation of 3D models of single cells (Fig
102   1B), allowing for subsequent quantitative analysis of ISGs (Fig S1). ISGs were segmented based on their
103   dense core in accordance with our previous work.[18,21] Size and LAC filters were applied to exclude
104   misattribution of lipid droplet and lysosomes. LysoTracker Red staining combined with Cryo-Fluorescence
105   microscopy demonstrated the presence of few, large lysosomes within the cell. Structured Illumination
106   Microscopy (SIM) imaging of GRINCH cells (INS-1 cells expressing hPro-CpepSfGFP) further confirmed
107   minimal overlap between ISGs and lysosomes (Fig. S2A-C). Our dataset included ~37,000 ISGs across
108   44 cells

109   ISG maturity was quantified using the mean LAC value of each ISG, with higher LAC values indicating
110   denser ISGs. ISG LAC can be used as a proxy for ISG maturity as dense, core-containing ISGs are
111   predicted to have higher LAC than less dense immature ISGs.[38] Pooling all ISGs from our dataset, we
112   observed a wide distribution in ISG mean LAC values (0.2 µm^{-1} - 0.55 µm^{-1}) (Fig S3A). This allowed us to
113   visualize a spectrum of ISG maturity indicating ISGs at different points in their maturation lifecycle (Fig 1C
114   and Fig S3C). The ability of SXT to track ISG location and maturity allowed us to visualize the spatial
115   distribution of ISG maturity in single cells (Fig 1D). We also observed that ISG size tremendously varied,
116   with a mean ISG diameter of 159 nm (Fig S3B). Overall, our imaging pipeline enabled detailed mapping
117   of ISG structure and maturity at a single cell level (*Video* S1).

118
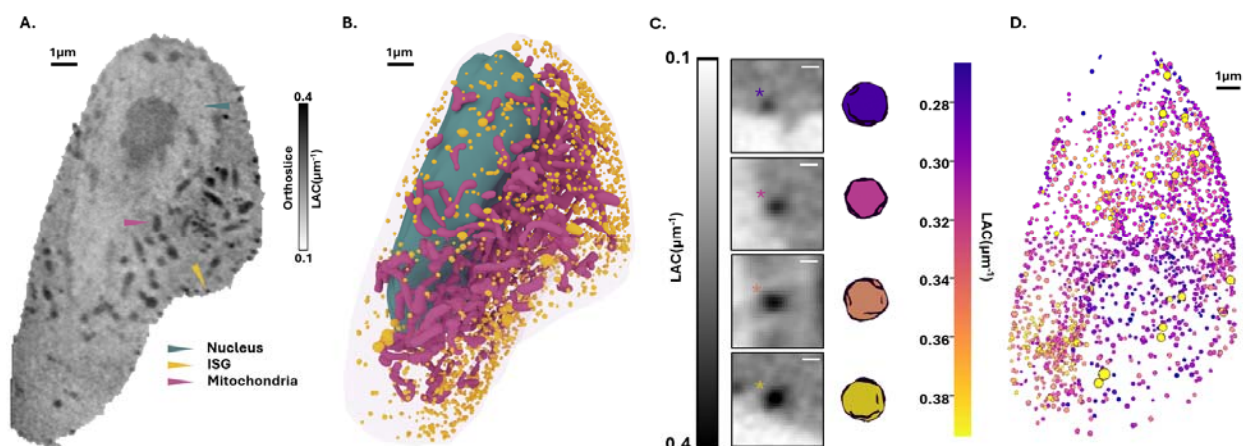
Figure 1. Using SXT as a tool to study ISG maturation.
120   (A) Orthoslice of a representative SXT tomogram through the XY-plane, with different organelles
121   identified by morphology and LAC values as follows: Nucleus – Teal arrowhead, ISG – yellow arrowhead,
122   and mitochondria – mauve arrowhead (B) 3D model of whole cell generated using the segmented masks
123   from the SXT tomograms in (A). (C) Left - Range of ISG maturities based on mean ISG LAC values. Right
124   – 3D rendering of corresponding ISG classes color coded based on their LAC values (D) A 3D model of
125   the spatial distribution of ISG maturity. ISGs are color coded by their maturity levels as shown in (C).

126

### *Conventional secretory stimuli impact ISG maturation.*

128   We assessed the effect of secretory stimuli on ISG maturation by stimulating INS-1E cells with six
129   different stimuli to obtain 44 whole cell reconstructions (Fig S4A-G). We captured tomograms at a 30-
130   minute time point after stimulation, focusing primarily on the more prolonged second phase of insulin
131   secretion.[39] To determine ISG molecular density, we analyzed ISGs from 5 to 7 whole cells per condition,
132   resulting in an average of 825 ISGs per cell and 5,200 ISGs per condition. To compare ISG maturation
133   across conditions, we used the mean ISG label field LAC for each cell, calculated by pooling all voxels

134 assigned to the segmented ISG label field and computing their mean. We stimulated INS-1E cells using
135 high glucose (HG) to model glucose-stimulated insulin secretion (GSIS). Since conventional secretory
136 stimuli enhance preexisting GSIS[11,39], they were costimulated along with HG. Consistent with prior
137 studies[39–43] all stimuli increased insulin secretion, as measured by an Enzyme-linked immunosorbent
138 assay (ELISA) (Fig 2B).

139 To assess the effect of conventional K_{ATP} channel blockers, we used glimepiride, a clinically approved
140 sulfonylurea drug for T2D.[40]There was no significant difference in ISG density between Glimepiride-
141 treated cells and the unstimulated or HG-only groups (Fig 2C), suggesting that membrane depolarization
142 alone does not influence ISG maturation. This finding was consistent with our previous results, which
143 showed that potassium chloride (a depolarization agent) stimulation increases secretion without affecting
144 ISG density [18]. We tested GKA-50, a glucokinase activator that increases metabolic flux by catalyzing the
145 phosphorylation of glucose to glucose-6-phopshate (G6P).[41] GKA-50 resulted in a significant increase in
146 ISG density (Fig 2C), indicating that glucokinase activation does affect ISG maturation. To explore free
147 fatty acid receptor 1 (FFAR1) related pathways, we tested TAK-875, a GPR40 agonist, working mainly via
148 $G_{\alpha q}$ and subsequent inositol triphosphate (IP_3) and diacylglycerol (DAG) signaling.[42,44] Like GKA-50, TAK-
149 875 treatment significantly increased ISG density (Fig 2C). To investigate incretin-based stimuli, we
150 stimulated INS1E cells with Exendin-4 (Ex-4), a Glucagon-like Peptide-1 receptor (GLP-1R) agonist, or
151 Gastric Inhibitory Polypeptide (GIP), a GIP receptor (GIPR) agonist. Both Ex-4 and GIP activate $G_{\alpha s}$ and
152 subsequent cyclic-Adenosine monophosphate (cAMP) signaling.[43] As we expected, we observed a
153 significantly higher ISG density in both Ex-4 and GIP treated cells compared to unstimulated cells (Fig
154 2C).

155 To determine whether the stimuli, in addition to affecting ISG density, also affected the insulin to
156 proinsulin (I:P) ratios, we measured secreted and intracellular insulin and proinsulin using ELISAs. In the
157 secreted media, Ex-4 and GIP stimulation caused the most significant increase in the I:P ratio, indicating
158 more mature ISGs being secreted (Fig 2D). Interestingly, the intracellular I:P ratios did not mirror this
159 trend. GKA-50 and Ex-4 significantly increased the I:P ratio as compared to the unstimulated cells, with
160 GKA-50 having the most significant effect, whereas GIP stimulation caused no significant change in the
161 I:P ratio compared to unstimulated cells (Fig 2E). We also observed a difference in the number of ISGs
162 present per cell across conditions (Fig S4H). We found a higher number of ISGs in HG-only cells as
163 compared to unstimulated cells. Co-stimulation with Glimepiride, GKA-50, and Ex-4, all resulted in a slight
164 reduction in ISG numbers as compared to HG-only cells, whereas GIP costimulation with HG led to the
165 highest number of ISGs. The decreased I:P ratio and increased number of ISGs with GIP stimulation
166 compared to Ex-4 potentially suggest differences in the intracellular actions of these two incretins on ISG
167 maturation, despite their similarities in secreted insulin levels and I:P ratios. To characterize the broader
168 effects of the secretory stimuli on cellular architecture, we also investigated the volumes and molecular
169 densities of other organelles (Table S1). Taken together, our results suggest that HG-only and
170 Glimepiride, increase insulin secretion without significantly affecting ISG maturation. In contrast,
171 glucokinase activation and GPR40, GLP-1R and GIPR agonism, significantly affect both insulin secretion
172 and ISG maturation.
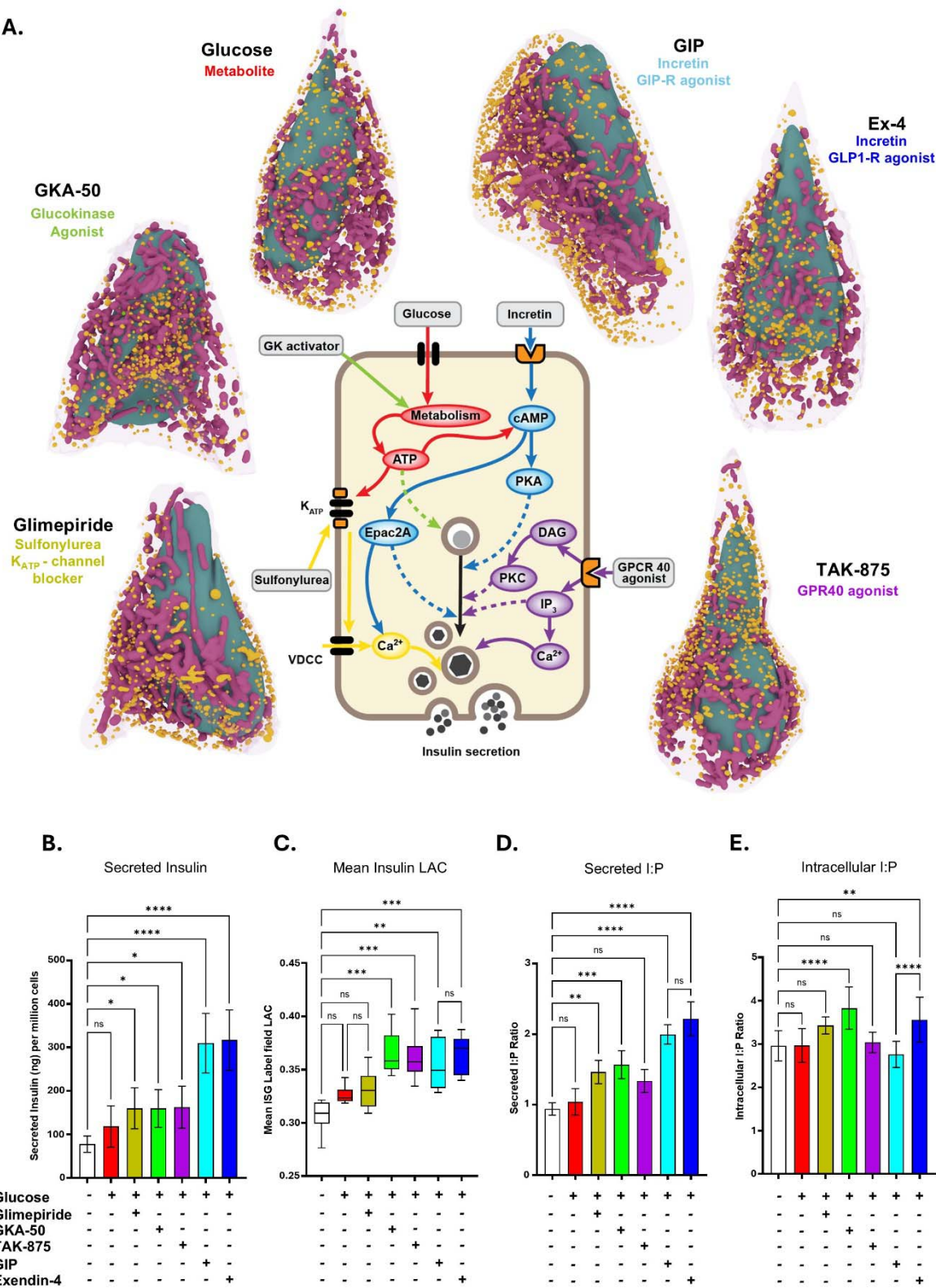
Figure 2. Impact of secretory stimuli on ISG density and insulin to proinsulin ratio.

(A) Central figure shows the mechanism of action and the cellular signaling pathways that are activated by the different classes of secretory stimuli. Representative whole cell 3D models generated from SXT

177 tomograms of cells treated with: Glimepiride (Yellow), GKA-50 (Green), Glucose (Red), GIP (cyan), Ex-4
178 (Blue), and TAK-875 (Purple) (B) Comparison of insulin secreted upon stimulation using ELISA shows
179 increased secretion levels upon stimulation. (n = 8 biological replicates) (C) Mean Insulin label field LAC
180 value comparison show distinct effects of the stimuli on label field ISG density (n = 5 to 7 cells) (D-E)
181 Ratio of Insulin to Proinsulin (I:P) upon stimulation: (D) secreted ratio (n = 4 biological replicates) (E)
182 intracellular ratio (n = 11 biological replicates). Error bars in all panels represent SDs. *p<0.05; **p<0.01:
183 ***p<0.001; ****p<0.0001 as calculated by a One-way ANOVA with Bonferroni's correction in all panels.

184

185 ***Distinct ISG Maturation Stimuli Drive Unique Structural Remodeling of ISGs.***

186 To further explore the unique effects of the stimuli on ISG maturation we evaluated individual ISG
187 structural parameters rather than mean ISG label field LAC. Larger, high-LAC ISGs may mask subtle LAC
188 differences among individual ISGs (Fig S5A-B). For example, GIP-treated cells showed more
189 heterogeneity in ISG density and size compared to Ex-4-treated cells despite similar mean ISG label field
190 LAC (Fig 2C) and insulin secretion (Fig 2B). SXT is ideal for capturing the structural and biophysical
191 characteristics of individual ISGs[20], providing a robust framework to observe heterogeneity in ISG
192 maturation under different conditions.

193 We found that different stimuli influenced ISG biophysical properties in distinct ways (Fig 3A). HG-only
194 and unstimulated ISGs exhibited significantly different mean ISG LACs (0.298 μm^{-1} and 0.311 μm^{-1},
195 respectively), accompanied by a slight but significant increase in mean diameter (167 nm and 169 nm,
196 respectively) (Fig 3B). Glimepiride stimulation, compared to unstimulated ISGs resulted in a significant
197 increase in mean ISG LAC (0.316 μm^{-1}). Compared to HG-only-stimulated ISGs, Glimepiride stimulation
198 did not cause a significant change in ISG LAC, with the mean values for both conditions being very
199 similar (Fig 3B). When stimulated with GKA-50, ISGs showed a significantly lower mean diameter (145
200 nm) alongside a significantly higher mean ISG density (0.345 μm^{-1}), suggesting a denser, more compact
201 biophysical state (Fig 3C). This trend mirrors reports in literature suggesting that mature ISGs are typically
202 denser and smaller in size compared to immature ISGs.[45,46] TAK-875 stimulation resulted in a significant
203 increase in mean ISG LAC (0.348 μm^{-1}), accompanied by an increase in mean diameter (172 nm) (Fig
204 3D). As GPR40 activation is associated with lipid signaling we also investigated whether TAK-875
205 stimulation caused a change in LD numbers (Fig S5C-D). We observed that there was no significant
206 difference in the number of LDs between the unstimulated and TAK-875 treated cells (Fig S5E). Ex-4
207 stimulation led to both significantly higher mean ISG density (0.347 μm^{-1}) and a reduced mean diameter
208 (143 nm) similar to GKA. On the other hand, GIP stimulation resulted in a slight increase in mean ISG
209 LAC (0.316 μm^{-1}) and a reduced mean diameter (147 nm) (Fig 3E). The ISG density for GIP-treated ISGs
210 obtained via analyzing individual ISGs (0.316 μm^{-1}) was different than the one obtained by analyzing the
211 label field (0.356 μm^{-1}). The reduced mean ISG LAC in conjunction with the reduced I:P ratio, indicates
212 that GIP might not be affecting ISG maturity as significantly as Ex-4. The reduction in diameter of the GIP-
213 treated ISGs could point towards an intermediate dense state before the ISG mature completely.

214 We defined an ISG biomaterial amount index (BAI), a variable encompassing both volumetric and
215 densitometric features. GIP treatment caused the largest S.D in the BAI indicating heterogeneity in the
216 amount of biomaterial in GIP-treated ISGs (Fig S6A). Additionally, we found that TAK-875 treated ISGs
217 had the highest BAI, while the GIP, GKA-50 and Ex-4 treated ISGs had significantly higher BAIs as
218 compared to unstimulated cells (Fig S6B). Additional ISG biophysical properties (Fig S6C) were affected
219 by the stimuli. Each ISG consists of multiple voxels, each with a unique LAC value, enabling the creation
220 of a distinct LAC histogram for every ISG.[20] These parameters offer insights into differences in the
221 structural organization and internal molecular distribution of ISG contents. The minimum, 25th percentile,
222 median, 75th percentile, and maximum ISG LAC all have the same trends as the mean ISG LAC (Fig
223 S6D-H). Due to changes in the biophysical makeup of the dense core upon stimulation, we also observed
224 differences in skew, kurtosis, and standard deviation of the ISGs (Fig S6I-K). ISGs treated with GKA-50,
225 and Ex-4 had the highest skew and the lowest kurtosis, suggesting that these parameters, in addition to

226   mean ISG LAC, could serve as differentiating factors between mature and immature dense cores.
227   Additionally, Ex-4 and GIP treated ISGs had significantly different skew and kurtosis values. Taken
228   together, our results reveal that secretory stimuli distinctly alter ISG structural properties and influence the
229   biophysical properties of ISG subpopulations.

230
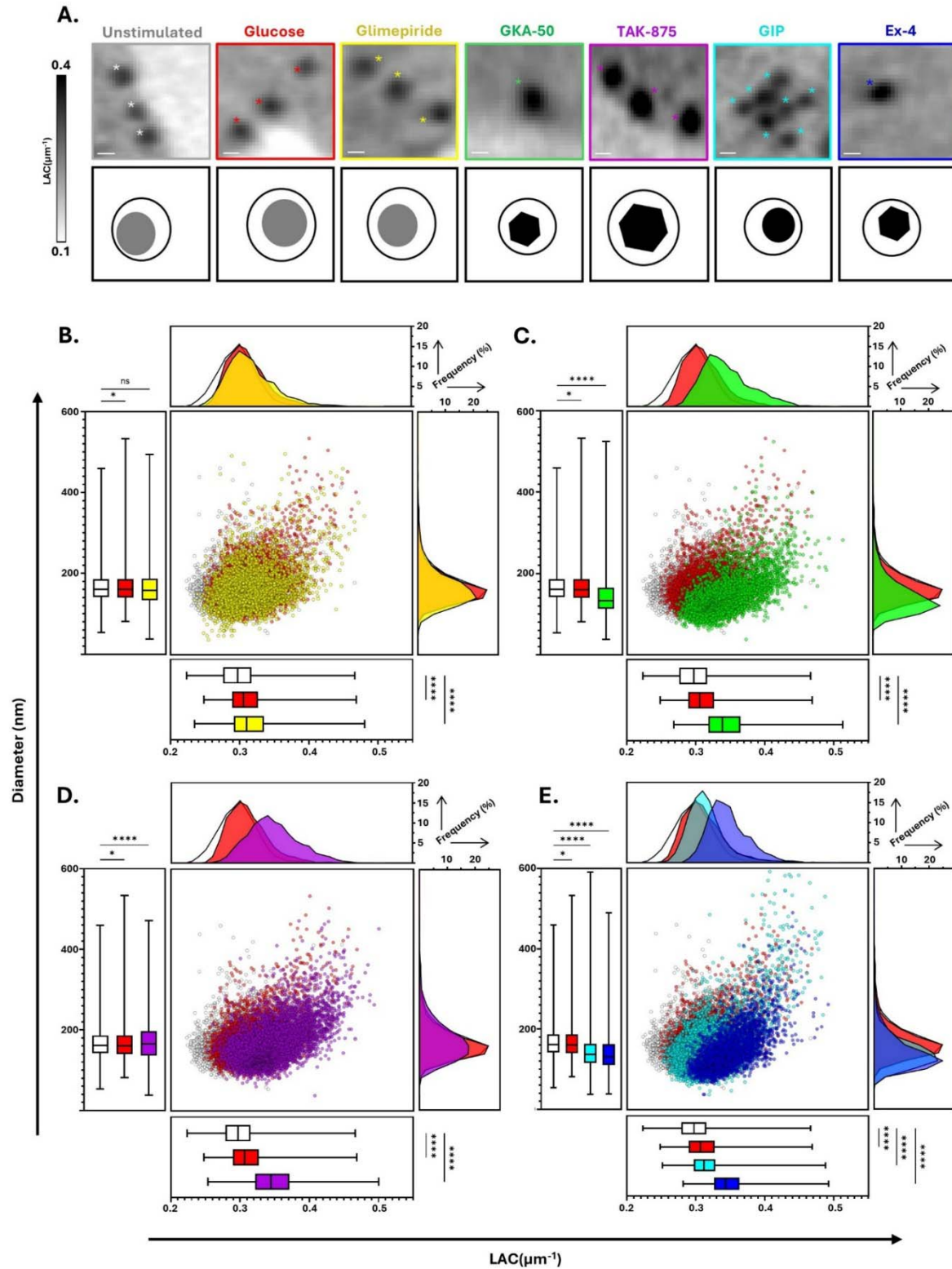
Figure 3. Change in structural and biophysical characteristics of ISGs under maturation stimuli.
(A) Top – representative orthoslice insets of ISGs under the influence of the different stimuli show variations in size and ISG LAC. Bottom – ISG graphic renderings of the ISGs on top show differences in

234 core size and density as reflected by black crystalline cores for conditions affecting maturation the most
235 and shaded gray dense cores for stimuli not significantly increasing maturation. (B-D) Mean ISG LAC
236 versus ISG diameter plot for pooled ISGs in a condition. Each point represents a single ISG. ISG LAC
237 and Diameter distribution is shown in histogram plots. Mean ISG LAC and ISG Diameter along with
238 comparison in these parameters between conditions shown in box and whisker plots. As compared to
239 ISGs from Unstimulated (white) (n = 5918) and Glucose-treated (Red) (n=4750) cells, ISGs from: (B)
240 Glimepiride-treated (yellow) (n = 4359) cells show a slight shift in ISG LAC and diameter; (C) GKA-50-
241 treated (n = 4044) (green) cells (show an increase in ISG LAC and decrease in diameter; (D) TAK-875
242 (purple) treated (n = 5506) cells show an increase in ISG LAC and in ISG diameter; (E) GIP (cyan) (n =
243 8363), and Ex-4-treated (n = 3362) cells (blue), show an greater increase in ISG LAC for Ex-4 as
244 compared to GIP and similar decrease in ISG diameter for both conditions.*p<0.05; **p<0.01: ***p<0.001;
245 ****p<0.0001 as calculated using a One-way ANOVA with Dunnet's correction.
246

Spatial distribution of ISG maturation.

248 To understand how different stimuli impact the localization of ISGs we determined the spatial distribution
249 of ISGs within cells. Typically there is an abundance of ISGs either docked or positioned near the
250 membrane (docked ISGs and readily releasable pool (RRP), respectively).[16,47,48] Once the initial pool of
251 ISGs is depleted, internal ISGs are recruited peripherally to fuel the second, more prolonged phase of
252 insulin secretion (Fig 4A).[49,50] We divided cells into seven distinct spatial zones, demarcated by a 0.1
253 change in the normalized Euclidean distance transform (EDT), with the first zone (EDT: 0 - 0.1) being the
254 cell periphery and the last zone representing cell interior (EDT: greater than 0.6) (Fig 4A). We observed
255 expected trends, with the majority of ISGs in the unstimulated condition at the cell membrane with a
256 smaller proportion of ISGs deeper inside the cell. Under HG stimulation, we observed a shift in the ISG
257 population towards the interior of the cell, with fewer ISGs present near the membrane. This reflects
258 secretion of docked ISGs and the RRP along with the maturation and mobilization of interior ISGs (Fig
259 S7A).

260 Costimulation with Glimepiride led to a sharp increase in ISGs near the membrane compared to the
261 unstimulated condition (Fig S7A). GKA-50 costimulation resulted in a distribution pattern similar to that of
262 unstimulated cells (Fig S7B). In contrast, under TAK-875 costimulation, the distribution of ISGs was
263 similar to that observed under HG-only stimulation (Fig S7C). The effects of HG and TAK-875 on ISG
264 positioning may be due to secretion of both docked ISGs and the RRP getting secreted during the first
265 phase of insulin secretion, resulting in fewer ISGs near the cell periphery as compared to unstimulated
266 cells. Despite Glimepiride and GKA-50 stimulating similar levels of insulin secretion as TAK-875, the
267 difference in ISG positioning under these conditions potentially indicates the ability of Glimepiride and
268 GKA-50 to replenish peripheral RRP stores. Finally, stimulation with GIP and with Ex-4, both reduced the
269 percentage of ISGs at the cell periphery and increased the abundance of the ISGs towards cell interior
270 (Fig S7D). The abundance of ISGs towards the cell interior hints towards a replenishment of internal ISG
271 stores through the synthesis or maturation of nascent ISGs thought to be present in the perinuclear
272 region[46].

273 The differences in ISG localization within the cell reflect the ability of distinct signaling pathways to
274 mobilize and redistribute distinct ISG pools. Since these ISG pools exhibit varying levels of maturity, we
275 used mean LAC values to determine the spatial distribution of ISG maturity in the cell. The periphery
276 (EDT: 0 - 0.1) contained the largest number of ISGs with the numbers progressively decreasing deeper
277 into the cell. Unstimulated ISGs had the lowest mean ISG LAC in each EDT zone (Fig 4B-E). Upon HG
278 stimulation, the ISG LAC trend changed, with the most internal ISGs displaying a high mean LAC, with
279 the values decreasing towards the periphery, where ISGs exhibited the lowest LAC (Fig 4B). Parallel to
280 HG, Glimepiride caused a similar increase in mean ISG LAC as compared to unstimulated ISGs across
281 most EDT zones. However, there was no significant difference in ISG LAC between the HG-only and
282 Glimepiride conditions within the 0.1 - 0.6 EDT range (Fig 4B). HG slightly increased the mean LAC of the

283   most internal ISGs as compared to Glimepiride-stimulated ISGs. Additionally, at the periphery,
284   Glimepiride significantly increased the mean LAC of the ISGs as compared to HG alone.

285   GKA stimulation, significantly increased ISG LAC values across all EDT zones, with the least significant
286   increase observed in the cell interior (Fig 4C). ISG density increased from interior progressively towards
287   the membrane, peaking in the 0.4 - 0.5 EDT zone, before decreasing towards the periphery. TAK-875
288   stimulation caused a substantial upward shift in the LAC profile as compared to HG-treated ISGs, with all
289   EDT zones showing significantly higher ISG LAC values (Fig 4D). Interestingly, the TAK-875 treated-ISGs
290   had relatively lower LAC values for the internal ISGs, which progressively increased in maturity towards
291   the periphery. In the case of GIP and Ex-4, we observed significant differences in mean ISG LAC across
292   all EDT zones (Fig 4E). There was no statistical difference in ISG LAC in most EDT zones between HG-
293   treated and GIP-treated ISGs. In contrast, Ex-4 stimulation caused a significant increase in ISG LAC in all
294   EDT zones compared to HG-treated ISGs. The decrease in ISG LAC right at the periphery (EDT: 0 - 0.1)
295   seen across all the conditions, may be due to docked ISGs actively releasing insulin, causing the dense
296   cores to dissolve. Another possibility is the occurrence of ISGs that have undergone kiss-and-run
297   exocytosis[51], resulting in progressively decreasing secretory material from ISGs.

298   When focusing on docked ISGs and the RRP at the cell periphery (EDT: 0 - 0.1), we found that TAK-875,
299   GKA-50, and Ex-4-treated ISGs had significantly higher mean LACs compared to unstimulated and HG-
300   only treated ISGs (Fig S7E). This was the same trend as the mean ISG LAC obtained for all ISGs. We
301   observed opposing trends when we analyzed internal ISGs (EDT greater than 0.1). TAK-875, GKA-50,
302   and Ex-4-treated ISGs showed significantly higher LACs compared to unstimulated and HG-only treated
303   cells, while HG-only, Glimepiride, and GIP-treated cells had significantly lower mean ISG LACs compared
304   to unstimulated ISGs (Fig S7F). Taken together, this suggests that distinct stimuli regulate both the
305   availability of ISGs at the cell membrane and their maturation state in the interior of the cell.
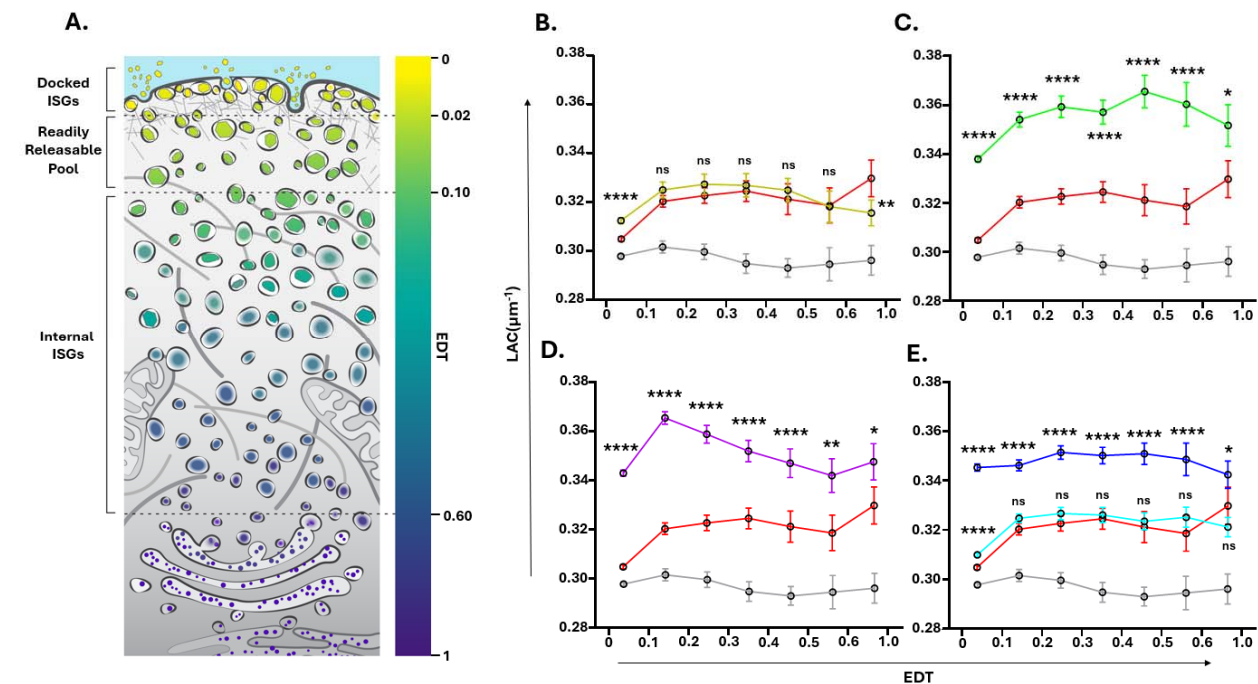

306
307   **Figure 4. Secretory stimuli cause shifts in ISG spatial distribution.**
308   (A) Cartoon rendering of the ISG maturation pathway with the ISGs color coded based on location with
309   respect to cell membrane. Normalized Euclidean distance transform (EDT) scale on the right indicates
310   where the ISG is located (EDT: 0 – At the cell membrane; EDT: 1 - furthest from the cell membrane).
311   Different ISG subpopulations are defined based on spatial localization through the normalized EDT:
312   Docked ISGS (EDT: 0 – 0.02), Readily Releasable Pool (RRP) (EDT: 0.02 - 0.10) and Internal ISGs or

313   Reserve Pool (EDT: 0.1 - 0.6). (B-E) ISG LAC distribution for each 0.1 EDT zone shows distribution of
314   ISG LAC across the cell. The last EDT zone is from 0.6 to 1.0. Each point represents the mean LAC of
315   the ISGs for the corresponding condition in that specific EDT range. Error bars represent 95% CI. As
316   compared to ISGs from glucose-only treated (red) cells, ISGs from: (B) Glimepiride treated cells (yellow)
317   mostly show no significant change in ISG LAC values or trends as compared to ISGs from glucose-only
318   treated cells (red). (C) GKA-50 treated cells (green) show a significant difference in LAC values (D) TAK-
319   875 treated cells (purple) show a significant difference in LAC values and an upward trend in LAC going
320   towards the membrane. (E) GIP treated cells (cyan) show no significance in LAC and Ex-4 treated cells
321   (blue) show a significant increase in LAC. Two-way ANOVA used as a statistical test for (B-E). *$p<0.05$;
322   **$p<0.01$: ***$p<0.001$; ****$p<0.0001$
323

324   ***ISG maturation in Primary Mice β-cells.***

325   As common in the β-cell biology field, we validated our findings in a more physiological context by
326   examining the effect of Ex-4 stimulation on ISG maturation in primary mouse β-cells (Fig 5A-B). Mouse β-
327   cells, isolated and co-stimulated with glucose (16.7 mM) and Ex-4 (10 nM), were larger and contained
328   more ISGs compared to INS-1E cells (Fig S8A-B). The mean ISG LAC of unstimulated β-cells (0.31 μm^{-1})
329   was similar to that of unstimulated INS-1E cells (0.3 μm^{-1}) (Fig S8C), and their diameter (166 nm) closely
330   matched that of INS-1E ISGs (167 nm) (Fig S8D). Upon Ex-4 stimulation, β-cells showed a sharp
331   increase in ISG density (Fig 5A), with a significant rise in mean ISG LAC (0.34 µm-1) and a slight
332   increase in ISG diameter (170 nm) (Fig 5C). Analysis of mean ISG LAC across different EDT zones (Fig
333   5D) revealed that Ex-4 stimulation increased LAC in all zones, similar to observations in INS-1E cells (Fig
334   4A-B and Fig 5D). Ex-4 stimulation also increased the intracellular I:P ratio at a 30-minute timepoint (Fig
335   5E).
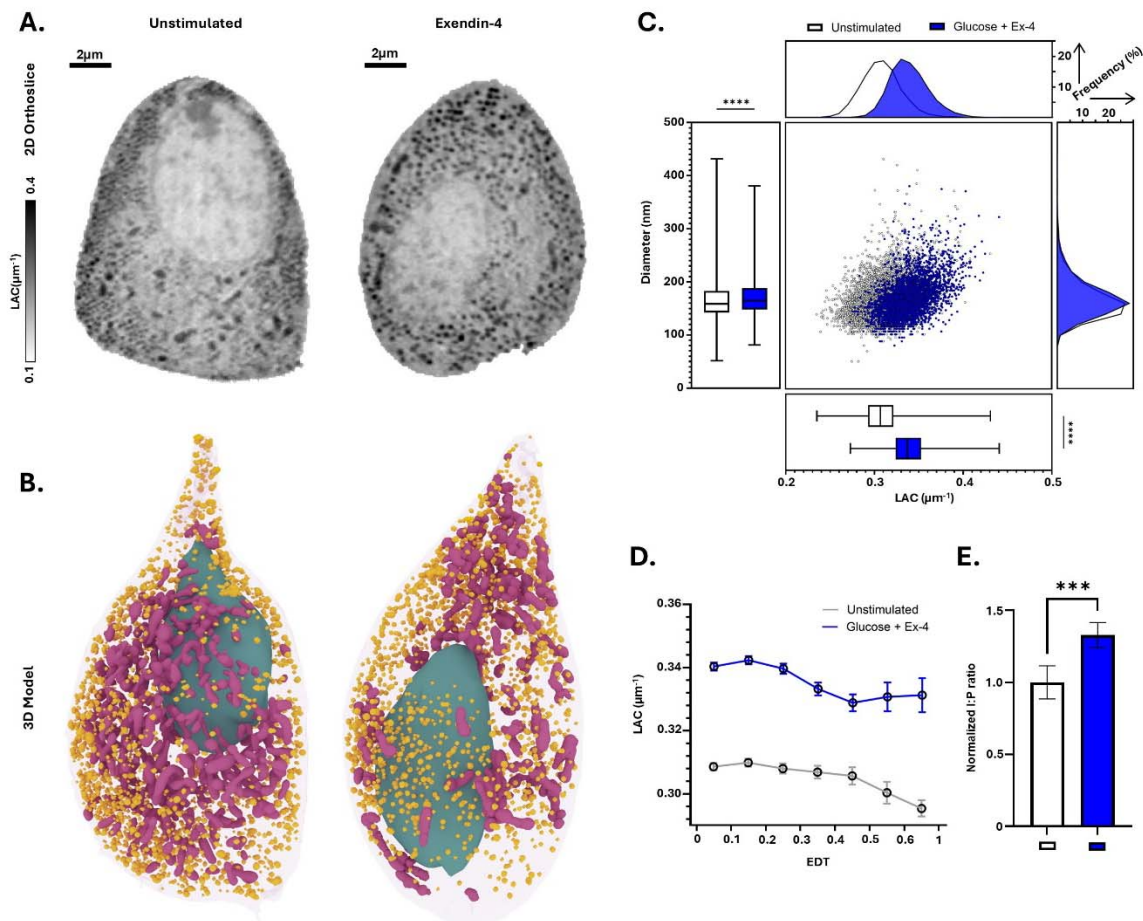
Figure 5. Ex-4 promotes ISG maturation in primary mouse β-cells.
(A) 2D X-Y orthoslice of representative SXT tomograms from primary mouse β-cells. Left – Unstimulated cells. Right – Glucose + Ex-4 treated cell showing denser, higher LAC ISGs. (B) 3D model of whole cells generated using the segmented masks from the respective SXT tomograms in (A) with ISGs in yellow, mitochondria in mauve and nuclei in teal. (C) ISG diameter vs mean ISG LAC plot for pooled primary mouse β -cell ISGs. Each point represents a single ISG. ISG LAC and diameter distribution is shown in histogram plots. Mean ISG LAC and ISG diameter along with comparison in these parameters between conditions shown in box and whisker plots. As compared to ISGs from Unstimulated (white) (n = 4528) cells, ISGs from Ex-4 treated (n = 3655) cells show a significantly higher ISG LAC value. (D) ISG LAC distribution for each 0.1 EDT zone shows distribution of ISG LAC across the cell. The last EDT zone is from 0.6 to 1.0. Each point represents the mean LAC for the corresponding condition in that specific EDT range. Error bars represent 95% CI. As compared to ISGs from unstimulated (grey) cells, ISGs from Ex-4 treated cells show a slightly more upward LAC trend travelling towards the periphery and significant differences in mean ISG LAC across all EDT zones. Error bars represent 95% CI. (E) Intracellular ratio of Insulin to Proinsulin (I:P) upon stimulation (n = 2 biological replicates, with 3 technical replicates each). Welch's t-test used as statistical test for (C) and (E). Error bars represent SDs. (A-E) *p<0.05; **p<0.01: ***p<0.001; ****p<0.0001.

DISCUSSION

In this work, we leveraged SXT to quantitatively map ISG structural parameters including ISG size, morphology, density and subcellular localization. We demonstrated that the activation of Glucokinase, GIPR, GLP-1R, and GPR40 drive ISG maturation at a 30-minute timepoint. Through unique changes in the biophysical parameters of IGSs we show that these signaling pathways remodel ISGs in distinct

360   ways. Additionally, we provide critical insights into how different stimuli alter overall cellular structure by
361   localizing ISG subpopulations within single cells.

Metabolic Signaling.

363   Under HG stimulation, we observed an increase in insulin secretion, but only a minor increase in the
364   molecular density of ISGs and no difference in the I:P ratios. Glucose plays several roles in regulating
365   insulin secretion. It depolarizes β-cells, aiding in insulin secretion[39], promotes insulin gene expression[52],
366   and post translationally regulates insulin mRNA condensates[53], thereby activating translation. However,
367   few reports have addressed its role in modulating ISG maturation. Previous work has shown that glucose
368   lowers ISG pH, acidifying the luminal environment.[23,54,55] This acidification catalyzes prohormone
369   convertases and carboxypeptidases, which are critical for proinsulin processing [56]. Here, we found that
370   glucose stimulation leads to a depletion of docked ISGs, and the RRP located at the periphery of the cell.
371   This depletion of potentially acidified ISGs, coupled with a slight increase in the mean ISG LAC, suggests
372   that while glucose influences basal ISG maturation, its effects are not as pronounced as those observed
373   with other secretory stimuli. Upon GKA-50 co-stimulation, we observed a significant increase in the mean
374   ISG LAC and slight reduction in ISG diameter. These changes, coupled with an increase in the I:P ratio,
375   suggest that glucokinase activation promotes ISG maturation. As high glucose levels can burden the
376   cellular metabolic machinery, glucokinase (GK) activation has been reported to alleviate metabolic stress
377   by enhancing the efficiency of glucose utilization, converting it into ATP.[57] This increased ATP production
378   may assist in acidifying ISGs via V-ATPase proton pumps located on their membranes.[58]

Membrane Depolarization.

380   Under Glimepiride co-stimulation, we observed no significant difference in the mean ISG LAC compared
381   to HG-only stimulation, despite an increase in insulin secretion. There was a significant increase in the
382   secreted I:P ratio, but no significant change in the intracellular I:P ratio. Glimepiride primarily exerts its
383   secretory effect by blocking K_{ATP} channels, causing membrane depolarization and subsequent ISG
384   fusion.[40] Consistent with our previous findings using potassium chloride, membrane depolarization alone
385   is unlikely to induce changes in ISG maturation. This is further supported by reports that depolarization-
386   based agents do not acidify ISGs and cause non-specific secretion of ISGs irrespective of their pH.[23] We
387   observed a high proportion of ISGs at the periphery under Glimepiride stimulation suggesting non-specific
388   recruitment of ISGs near the membrane irrespective of maturity. This observation is notable, as some
389   reports have suggested that long-term sulfonylurea treatment may result in lower I:P ratios.[59] A limitation
390   of our current interpretation is that Glimepiride, like other sulfonylureas, may also act via Epac2, in
391   addition to its depolarizing effect.[60] Epac2 is a known downstream target of incretin-based secretory
392   stimuli, and the combination of sulfonylureas with GLP-1 agonists leads to synergistic effects as
393   sulfonylureas uncouple incretins from glucose-dependency.[61] Future experiments involving dual
394   stimulation with incretins and sulfonylureas could help elucidate their combined effects on ISG
395   maturation.

GPR40 activation

397   Under TAK-875 stimulation, we observed an increase in insulin secretion alongside a rise in ISG
398   molecular density. Upon GPR40 activation, we anticipated some changes in ISG LAC, but did not
399   anticipate the significant increase in ISG diameter. The traditional view of ISG maturation suggests that
400   immature ISGs undergo significant lipid remodeling, becoming smaller and denser as they are trafficked
401   to the membrane.[46] Interestingly, in the TAK-875 condition, we observed a progressive increase in both
402   ISG diameter and LAC as ISGs trafficked from the cell interior to the periphery. Since GPR40 activation
403   primarily triggers G_{aq} signaling through IP_3 and DAG, key mediators of lipid signaling and exchange[42], we
404   hypothesize that the dual increase in ISG volume and density may result from lipid exchange, leading to
405   changes in lipid composition and ISG enlargement. Several studies have reported lipid exchange at
406   membrane contact sites (MCS) between organelles,[62,63] and lipid exchange at the ISG - endoplasmic
407   reticulum interface has also been found to fuel ISG maturation.[64] It is possible that ISG biochemical and

408 structural remodeling could occur via specific ISG membrane contact sites.[18,21,65] Sphingolipids may play
409 a key role in this process, as specific sphingolipid subtypes are known to influence proinsulin processing
410 and contribute to differences between ISG subpopulations.[66] The absence of a significant change in the
411 intracellular I:P ratio following TAK-875 treatment also suggests a distinct mechanism of ISG maturation
412 as compared to the other stimuli.

413 ### *Incretin Signaling.*

414 GIP and Ex-4 stimulation caused the most significant insulin secretion among all conditions due to the
415 ability of incretins to boost glucose-stimulated insulin secretion. Both GIP and Ex-4 exert their secretory
416 effects through $G_{\alpha s}$ signaling, which generates cAMP and activates downstream pathways via protein
417 kinase A (PKA) and Epac2.[43] Previous studies have demonstrated that Ex-4 promotes ISG acidification.[23]
418 In this study, we observed that Ex-4 enhanced ISG molecular density across multiple regions of the cell
419 and increased both the intracellular and secreted insulin-to-proinsulin (I:P) ratios. Taken together, we
420 expect that Ex-4 enhances ISG maturation by acidifying the granule lumen. While the detailed
421 mechanism mediating this ISG density increase remains unclear, PKA activation in other biological
422 systems can lead to phosphorylation of V-ATPase subunits leading to cellular compartment
423 acidification.[67,68] Alternatively, Epac2 activation has also been implicated in priming and acidifying docked
424 ISGs at the periphery just before secretion.[69] Additionally, GLP-1R interacts with multiple proteins such
425 as, ATP6ap2, a subunit of the V-ATPase. Activation of GLP-1R could affect acidification by regulation of
426 this subunit.[70] The effects on ISG density we observed could be a result of any combination of these
427 pathways.

428 We expected GIP to show effects comparable to Ex-4 because it activates similar downstream pathways.
429 We observed an increase in insulin secretion and the secreted I:P ratio, indicating that GIP promotes the
430 secretion of more mature ISGs. However, contrary to our expectations, GIP stimulation led to significantly
431 lower ISG density and intracellular I:P ratios compared to Ex-4. This suggests that while both incretins
432 stimulate insulin secretion similarly, they have distinct effects on ISG maturation. Notably, GIP stimulation
433 led to an increased number of ISGs and a reduction in ISG diameter, a hallmark of maturation. Although
434 the mean ISG LAC did not increase as significantly as with Ex-4, the presence of many more ISGs in the
435 GIP condition, along with the decrease in diameter, suggests that nascent ISGs may be undergoing early
436 stages of maturation. This indicates some maturation is occurring, but not to the same extent as in the
437 Ex-4 condition. Our observations may be linked to differences in expression levels of GLP-1R and GIP-R
438 in INS-1E cells, or to potentially subtlety distinct signaling events between the two receptors.[43]

439 GIPR and GLP-1R agonism are key therapeutic targets for diabetes and other metabolic diseases.[43,71,72]
440 Our findings are intriguing given reports that GIP-R and GLP-1R agonists significantly increase C-peptide
441 levels, I:P ratios, and overall β-cell health.[73,74] The split actions of the incretins are particularly fascinating
442 to think about in the context of dual agonism, wherein GLP-1R and GIPR agonists are co-
443 administered.[42,73] Future work could investigate whether dual stimulation with GIP and Ex-4 leads to
444 synergistic effects of an increase in ISG density coupled with an increase in the number of ISGs. These
445 results highlight the importance of further exploring the relationship between ISG maturation and insulin
446 secretion, particularly under the influence of various signaling pathways. We also show that the effects of
447 Ex-4 on increasing ISG density and enhancing I:P ratios are conserved in primary mouse β-cells. Notably,
448 Ex-4's impact on ISG density is observed throughout the entire β-cell, both at the periphery and interior.
449 These results validate that short-term activation of GLP-1R enhances ISG maturation during secretion in
450 primary mouse islets.

451 ### *Methodological Limitations*

452 Even though we hypothesize that the activation of the G-protein coupled receptors (GPCRs) (GLP-1R,
453 GIPR and GPR40) via their primary signaling pathways mentioned above cause changes in ISG
454 maturation, we cannot rule out the effect of β-arrestin signaling or other downstream signaling pathways
455 that might be responsible for this effect.[75] Notably, regulation of GPCRs through GRK6 activity has been

456 linked to enhanced proinsulin processing.[76] Although we can quantify whole-cell ISG distribution,
457 uncertainty remains as to whether we are visualizing all ISGs or primarily those with dense cores because
458 we observe fewer ISGs in primary mouse beta cells compared to other whole cell studies.[15,16]
459 Additionally, the ISG diameters we obtained are relatively smaller (159 nm for INS-1E and 166 nm for
460 primary mice β-cells) than those reported in other studies (greater than 300nm).[15,16,65] Interestingly, the
461 observed size is consistent with reports of core diameters[15] rather than overall ISG diameters, suggesting
462 we may be visualizing dense cores while missing the larger, less dense nascent ISGs.[38]

463 ***Future Directions***

464 To identify changes in the molecular machinery of the ISG subpopulations, an in depth proteomic and
465 lipidomic analysis will help define protein and lipid composition of the ISGs under the influence of different
466 maturation stimuli. Taken together, the field would have a stronger understanding of how the cell
467 regulates ISG subpopulations and define what their biological roles are. This is critical as some secretory
468 stimuli lead to secretion of multiple populations, while others secrete only specific populations. A basic
469 understanding of the effects of these drugs in single cell systems may pave the way to understand their
470 large-scale effects in complex organisms. The impact of defects in ISG maturation machinery[77–80] has
471 sparked a growing interest in how disruptions to ISG maturation affect disease.[73,74,81–83] The effect of
472 secretory stimuli on ISG structural remodeling raises the question of whether impairment in maturation
473 during disease alters ISG biophysical characteristics. Our approach could be used to determine if
474 structural remodeling occurs at different stages of disease progression. Finally, our approach can be
475 extended to other cell types, with similar dense core granule maturation systems to investigate hormone
476 maturation in a broader biological context.

477 **RESOURCE AVAILABILITY**

478 ***Lead contact***
479 Further information and requests for resources and reagents should be directed to and will be fulfilled by
480 the lead contact, Kate L. White (katewhit@usc.edu).

481 ***Materials availability***
482 This study did not generate new reagents.
483
484 ***Data and code availability***
485 All reconstructed tomograms are available upon request from corresponding author
486

487 **ACKNOWLEDGMENTS**

502 **AUTHOR CONTRIBUTIONS**

503 Conceptualization, A.D. and K.L.W.; methodology, A.D., V.L. and K.L.W.; Investigation, A.D., K.C., J.C.,
504 M.J.H.C., S.M., R.V., and V.L.; writing—original draft, A.D. and K.L.W.; writing—review & editing, A.D.,
505 K.C., J.C., M.J.H.C., S.M., R.V., S.G., V.L. and K.L.W.; funding acquisition, S.G., V.L. and K.L.W.;
506 resources, V.L. and K.L.W.; supervision, S.G., V.L. and K.L.W.

507 **DECLARATION OF INTERESTS**

508 The authors declare no conflict of interest.

509

510 **SUPPLEMENTAL INFORMATION**

511 **Document S1. Figures S1–S8 and Table S1** (this is the main PDF)
512 **Video S1. 3D cell mapping of ISG maturation using SXT, related to Figure 1**

513

514

515

516

517

REFERENCES

1. Petersen, M.C., and Shulman, G.I. (2018). Mechanisms of Insulin Action and Insulin Resistance. Physiological Reviews 98, 2133–2223.

2. Omar-Hmeadi, M., and Idevall Hagren, O. (2021). Insulin granule biogenesis and exocytosis. Cell. Mol. Life Sci 78, 1957–1970.

3. Suckale, J., and Solimena, M. (2010). The insulin secretory granule as a signaling hub. Trends in Endocrinology & Metabolism 21, 599–609.

4. Arvan, P., and Castle, D. (1998). Sorting and storage during secretory granule biogenesis: looking backward and looking forward. Biochemical Journal 332, 593–610.

5. Dodson, G., and Steiner, D. (1998). The role of assembly in insulin's biosynthesis. Current Opinion in Structural Biology 8, 189–194.

6. RØDER, M.E., PORTE, D.J., SCHWARTZ, R.S., and KAHN, S.E. (1998). Disproportionately Elevated Proinsulin Levels Reflect the Degree of Impaired B Cell Secretory Capacity in Patients with Noninsulin-Dependent Diabetes Mellitus. The Journal of Clinical Endocrinology and Metabolism 83, 604–608.

7. Rodriguez-Calvo, T., Chen, Y., Verchere, C.B., Haataja, L., Arvan, P., Leete, P., Richardson, S.J., Morgan, N.G., Qian, W., Pugliese, A., et al. (2021). Altered β-Cell Prohormone Processing and Secretion in Type 1 Diabetes. Diabetes (New York, N.Y.) 70, 1038–1050.

8. Sims, E.K., Bahnson, H.T., Nyalwidhe, J., Haataja, L., Davis, A.K., Speake, C., DiMeglio, L.A., Blum, J., Morris, M.A., Mirmira, R.G., et al. (2019a). Proinsulin Secretion Is a Persistent Feature of Type 1 Diabetes. Diabetes Care 42, 258–264.

9. Sims, E.K., Syed, F., Nyalwidhe, J., Bahnson, H.T., Haataja, L., Speake, C., Morris, M.A., Balamurugan, A.N., Mirmira, R.G., Nadler, J., et al. (2019b). Abnormalities in proinsulin processing in islets from individuals with longstanding T1D. Translational Research : The Journal of Laboratory and Clinical Medicine 213, 90–99.

10. Kalwat, M.A., and Cobb, M.H. (2017). Mechanisms of the amplifying pathway of insulin secretion in the β cell. Pharmacology & Therapeutics 179, 17–30.

11. Seino, S., Sugawara, K., Yokoi, N., and Takahashi, H. (2017). β-Cell signalling and insulin secretagogues: A path for improved diabetes therapy. Diabetes, Obesity & Metabolism 19, 22–29.

12. Davidson, H.W. (2004). (Pro)Insulin processing: A historical perspective. Cell Biochemistry and Biophysics 40, 143–157.

13. Lindberg, I., Lincoln, B., and Rhodes, C.J. (1992). Fluorometric assay of a calcium-dependent, paired-basic processing endopeptidase present in insulinoma granules. Biochemical and Biophysical Research Communications 183, 1–7.

14. Rafelski, S.M., and Marshall, W.F. (2008). Building the cell: design principles of cellular architecture. Nat Rev Mol Cell Biol 9, 593–602.

15. Pfeifer, C.R., Shomorony, A., Aronova, M.A., Zhang, G., Cai, T., Xu, H., Notkins, A.L., and Leapman, R.D. (2015). Quantitative analysis of mouse pancreatic islet architecture by serial block-face SEM. Journal of Structural Biology 189, 44–52.

16. Müller, A., Schmidt, D., Xu, C.S., Pang, S., D'Costa, J.V., Kretschmar, S., Münster, C., Kurth, T., Jug, F., Weigert, M., Hess, H.F., and Solimena, M. (2021). 3D FIB-SEM reconstruction of microtubule-organelle interaction in whole primary mouse β cells. The Journal of Cell Biology 220,

17. Guo, J., and Larabell, C.A. (2019). Soft X-ray tomography: virtual sculptures from cell cultures. Current Opinion in Structural Biology 58, 324–332.

18. White, K.L., Singla, J., Loconte, V., Chen, J., Ekman, A., Sun, L., Zhang, X., Francis, J.P., Li, A., Lin, W., et al. (2020). Visualizing subcellular rearrangements in intact β cells using soft x-ray tomography. Science Advances 6,

19. Loconte, V., Chen, J., Vanslembrouck, B., Ekman, A.A., McDermott, G., Le Gros, M.A., and Larabell, C.A. (2023). Soft X-ray tomograms provide a structural basis for whole-cell modeling. The FASEB Journal 37, e22681–n/a.

20. Deshmukh, A., Chang, K., Cuala, J., Vanslembrouck, B., Georgia, S., Loconte, V., and White, K.L. (2024). Subcellular Feature-Based Classification of α and β Cells Using Soft X-ray Tomography. Cells (Basel, Switzerland) 13, 869.

21. Loconte, V., Singla, J., Li, A., Chen, J., Ekman, A., McDermott, G., Sali, A., Le Gros, M., White, K.L., and Larabell, C.A. (2022). Soft X-ray tomography to map and quantify organelle interactions at the mesoscale. Structure (London) 30, 510–521.e3.

22. Mirvis, M., Weingard, B., Goodman, S., and Marshall, W.F. (2025). A scoping study of the whole-cell imaging literature: a foundational corpus, potential for data-mining and research synthesis, and a call for standardization of an emerging field. bioRxiv

23. Lin, W., Tseng, K., Fraser, S.E., Junge, J., and White, K.L. (2024). Decoding Insulin Secretory Granule Maturation Using Genetically Encoded pH Sensors. ACS Sensors 9, 6032–6039.

24. Ivanova, A., Kalaidzidis, Y., Dirkx, R., Sarov, M., Gerlach, M., Schroth-Diez, B., Müller, A., Liu, Y., Andree, C., Mulligan, B., et al. (2013). Age-Dependent Labeling and Imaging of Insulin Secretory Granules. Diabetes (New York, N.Y.) 62, 3687–3696.

25. Yau, B., Hays, L., Liang, C., Laybutt, D.R., Thomas, H.E., Gunton, J.E., Williams, L., Hawthorne, W.J., Thorn, P., Rhodes, C.J., and Kebede, M.A. (2020). A fluorescent timer reporter enables sorting of insulin secretory granules by age. The Journal of Biological Chemistry 295, 8901–8911.

26. Yi, H., Gong, D., Daddysman, M.K., Renn, M., and Scherer, N.F. (2024). Distinct Sub- to Superdiffuse Insulin Granule Transport Behaviors in β-Cells Are Strongly Affected by Granule Age. The Journal of Physical Chemistry. B 128, 6246–6256.

27. Hoboth, P., Müller, A., Ivanova, A., Mziaut, H., Dehghany, J., Sönmez, A., Lachnit, M., Meyer-Hermann, M., Kalaidzidis, Y., and Solimena, M. (2015). Aged insulin granules display reduced microtubule-dependent mobility and are disposed within actin-positive multigranular bodies. Proceedings of the National Academy of Sciences 112, E667–E676.

28. Ferri, G., Digiacomo, L., Lavagnino, Z., Occhipinti, M., Bugliani, M., Cappello, V., Caracciolo, G., Marchetti, P., Piston, D.W., and Cardarelli, F. (2019). Insulin secretory granules labelled with phogrin-fluorescent proteins show alterations in size, mobility and responsiveness to glucose stimulation in living β-cells. Sci Rep 9, 2890.

29. Barekatain, M., Liu, Y., Archambeau, A., Cherezov, V., Fraser, S., White, K.L., and Hayes, M.A. (2024). Insulator-based dielectrophoresis-assisted separation of insulin secretory vesicles. eLife 13,

30. Norris, N., Yau, B., Famularo, C., Webster, H., Loudovaris, T., Thomas, H.E., Larance, M., Senior, A.M., and Kebede, M.A. (2024). Optimized Proteomic Analysis of Insulin Granules From MIN6 Cells Identifies Scamp3, a Novel Regulator of Insulin Secretion and Content. Diabetes (New York, N.Y.) 73, 2045–2054.

31. Neukam, M., Sala, P., Brunner, A., Ganß, K., Palladini, A., Grzybek, M., Topcheva, O., Vasiljević, J., Broichhagen, J., Johnsson, K., et al. (2024). Purification of time-resolved insulin granules reveals proteomic and lipidomic changes during granule aging. Cell Reports (Cambridge) 43, 113836.

32. Kreutzberger, A.J.B., Kiessling, V., Doyle, C.A., Schenk, N., Upchurch, C.M., Elmer-Dixon, M., Ward, A.E., Preobraschenski, J., Hussein, S.S., Tomaka, W., et al. (2020). Distinct insulin granule subpopulations implicated in the secretory pathology of diabetes types 1 and 2. eLife 9,

33. Brunner, Y., Couté, Y., Iezzi, M., Foti, M., Fukuda, M., Hochstrasser, D.F., Wollheim, C.B., and Sanchez, J. (2007). Proteomics Analysis of Insulin Secretory Granules. Molecular & Cellular Proteomics 6, 1007–1017.

34. Hickey, A.J.R., Bradley, J.W.I., Skea, G.L., Middleditch, M.J., Buchanan, C.M., Phillips, A.R.J., and Cooper, G.J.S. (2009). Proteins Associated with Immunopurified Granules from a Model Pancreatic Islet β-Cell System: Proteomic Snapshot of an Endocrine Secretory Granule. Journal of Proteome Research 8, 178–186.

35. Schvartz, D., Brunner, Y., Couté, Y., Foti, M., Wollheim, C.B., and Sanchez, J. (2012). Improved characterization of the insulin secretory granule proteomes. Journal of Proteomics 75, 4620–4631.

36. Li, M., Du, W., Zhou, M., Zheng, L., Song, E., and Hou, J. (2018). Proteomic analysis of insulin secretory granules in INS-1 cells by protein correlation profiling. Biophys Rep 4, 329–338.

37. Parkinson, D.Y., Knoechel, C., Yang, C., Larabell, C.A., and Le Gros, M.A. (2012). Automatic alignment and reconstruction of images for soft X-ray tomography. Journal of Structural Biology 177, 259–266.

38. Autin, L., Barbaro, B.A., Jewett, A.I., Ekman, A., Verma, S., Olson, A.J., and Goodsell, D.S. (2022). Integrative structural modelling and visualisation of a cellular organelle. QRB Discovery 3, e11.

39. Komatsu, M., Takei, M., Ishii, H., and Sato, Y. (2013). Glucose-stimulated insulin secretion: A newer perspective. Journal of Diabetes Investigation 4, 511–516.

40. LANGTRY, H.D., and BALFOUR, J.A. (1998). Glimepiride : A review of its use in the management of type 2 diabetes mellitus. Drugs (New York, N.Y.) 55, 563–584.

41. JOHNSON, D., SHEPHERD, R.M., GILL, D., GORMAN, T., SMITH, D.M., and DUNNE, M.J. (2007). Glucose-Dependent Modulation of Insulin Secretion and Intracellular Calcium Ions by GKA50, a Glucokinase Activator. Diabetes 56, 1694–1702.

42. Yamada, H., Yoshida, M., Ito, K., Dezaki, K., Yada, T., Ishikawa, S., and Kakei, M. (2016). Potentiation of Glucose-stimulated Insulin Secretion by the GPR40–PLC–TRPC Pathway in Pancreatic β-Cells. Sci Rep 6, 25912.

43. Seino, Y., Fukushima, M., and Yabe, D. (2010). GIP and GLP-1, the two incretin hormones: Similarities and differences. Journal of Diabetes Investigation 1, 8–23.

44. Negoro, N., Sasaki, S., Mikami, S., Ito, M., Suzuki, M., Tsujihata, Y., Ito, R., Harada, A., Takeuchi, K., Suzuki, N., et al. (2010). Discovery of TAK-875: A Potent, Selective, and Orally Bioavailable GPR40 Agonist. ACS Medicinal Chemistry Letters 1, 290–294.

45. Orci, L., Ravazzola, M., Amherdt, M., Perrelet, A., Powell, S.K., Quinn, D.L., and Moore, H.H. (1987). The trans-most cisternae of the Golgi complex: A compartment for sorting of secretory and plasma membrane proteins. Cell 51, 1039–1051.

46. Arvan, P., and Halban, P.A. (2004). Sorting Ourselves Out: Seeking Consensus on Trafficking in the Beta-Cell. Traffic (Copenhagen, Denmark) 5, 53–61.

47. DANIEL, S., NODA, M., STRAUB, S.G., and SHARP, G.W.G. (1999). Identification of the docked granule pool responsible for the first phase of glucose-stimulated insulin secretion. Diabetes 48, 1686–1690.

48. BRATANOVA-TOCHKOVA, T.K., CHENG, H., DANIEL, S., GUNAWARDANA, S., LIU, Y., MULVANEY-MUSA, J., SCHERMERHORN, T., STRAUB, S.G., YAJIMA, H., and SHARP,

G.W.G. (2002). Triggering and Augmentation Mechanisms, Granule Pools, and Biphasic Insulin Secretion. Diabetes 51, 83.

49. Dehghany, J., Hoboth, P., Ivanova, A., Mziaut, H., Müller, A., Kalaidzidis, Y., Solimena, M., and Meyer-Hermann, M. (2015). A Spatial Model of Insulin-Granule Dynamics in Pancreatic β-Cells. Traffic (Copenhagen, Denmark) 16, 797–813.

50. JUNE CHUNQIU HOU, LE MIN, and PESSIN, J.E. (2009). INSULIN GRANULE BIOGENESIS, TRAFFICKING AND EXOCYTOSIS. Vitamins and Hormones 80, 473–506.

51. Rutter, G.A., and Hill, E.V. (2006). Insulin Vesicle Release: Walk, Kiss, Pause ... Then Run. Physiology (Bethesda, Md.) 21, 189–196.

52. Poitout, V., Hagman, D., Stein, R., Artner, I., Robertson, R.P., and Harmon, J.S. (2006). Regulation of the Insulin Gene by Glucose and Fatty Acids. The Journal of Nutrition 136, 873–876.

53. Quezada, E., Vasiljevic, J., Pal, A., Münster, C., Friedland, D., Schöniger, E., Sönmez, A., Seiler, A., Roch, P., Wegbrod, C., et al. (2024). Post-transcriptional regulation of insulin mRNA storage by G3BP1/2+ condensates in beta cells. bioRxiv

54. Stiernet, P., Guiot, Y., Gilon, P., and Henquin, J. (2006). Glucose Acutely Decreases pH of Secretory Granules in Mouse Pancreatic Islets: MECHANISMS AND INFLUENCE ON INSULIN SECRETION. The Journal of Biological Chemistry 281, 22142–22151.

55. Fang, Y., Feng, H., Zhang, B., Zhang, S., Zhou, Y., Hao, P., Zhou, Z., Zhou, S., Li, N., Hui, Y., et al. (2024). Cytosolic pH is a direct nexus in linking environmental cues with insulin processing and secretion in pancreatic β cells. Cell Metabolism 36, 1237–1251.e4.

56. Hutton, J.C. (1994). Insulin secretory granule biogenesis and the proinsulin-processing endopeptidases. Diabetologia 37 Suppl 2, S48–S56.

57. Ashcroft, F.M., Lloyd, M., and Haythorne, E.A. (2023). Glucokinase activity in diabetes: too much of a good thing? Trends in Endocrinology and Metabolism 34, 119–130.

58. Sun-Wada, G., Toyomura, T., Murata, Y., Yamamoto, A., Futai, M., and Wada, Y. (2006). The a 3 isoform of V-ATPase regulates insulin secretion from pancreatic β-cells. Journal of Cell Science 119, 4531–4540.

59. Ohkura, T., Inoue, K., Fujioka, Y., Nakanishi, R., Shiochi, H., Sumi, K., Yamamoto, N., Matsuzawa, K., Izawa, S., Ohkura, H., et al. (2013). The proinsulin/insulin (PI/I) ratio is reduced by postprandial targeting therapy in type 2 diabetes mellitus: a small-scale clinical study. BMC Research Notes 6, 453–453.

60. Zhang, C., Katoh, M., Shibasaki, T., Minami, K., Sunaga, Y., Takahashi, H., Yokoi, N., Iwasaki, M., Miki, T., and Seino, S. (2009). The cAMP Sensor Epac2 Is a Direct Target of Antidiabetic Sulfonylurea Drugs. Science 325, 607–610.

61. DE HEER, J., and HOIST, J.J. (2007). Sulfonylurea Compounds Uncouple the Glucose Dependence of the Insulinotropic Effect of Glucagon-Like Peptide 1. Diabetes 56, 438–443.

62. Prinz, W.A. (2014). Bridging the gap: Membrane contact sites in signaling, metabolism, and organelle dynamics. Journal of Cell Biology 205, 759–769.

63. Petrungaro, C., and Kornmann, B. (2019). Lipid exchange at ER-mitochondria contact sites: a puzzle falling into place with quite a few pieces missing. Current Opinion in Cell Biology 57, 71–76.

64. Panagiotou, S., Tan, K.W., Nguyen, P.M., Müller, A., Oqua, A.I., Tomas, A., Wendt, A., Eliasson, L., Tengholm, A., Solimena, M., and Idevall-Hagren, O. (2024). OSBP-mediated PI(4)P-cholesterol exchange at endoplasmic reticulum-secretory granule contact sites controls insulin secretion. Cell Reports (Cambridge) 43, 113992.

65. Zhang, X., Carter, S.D., Singla, J., White, K.L., Butler, P.C., Stevens, R.C., and Jensen, G.J. (2020). Visualizing insulin vesicle neighborhoods in β cells by cryo–electron tomography. Science Advances 6,

66. Griess, K., Rieck, M., Müller, N., Karsai, G., Hartwig, S., Pelligra, A., Hardt, R., Schlegel, C., Kuboth, J., Uhlemeyer, C., et al. (2023). Sphingolipid subtypes differentially control proinsulin processing and systemic glucose homeostasis. Nat Cell Biol 25, 20–29.

67. Al-bataineh, M.M., Gong, F., Marciszyn, A.L., Myerburg, M.M., and Pastor-Soler, N.M. (2014). Regulation of proximal tubule vacuolar H+-ATPase by PKA and AMP-activated protein kinase. American Journal of Physiology-Renal Physiology 306, 981.

68. Alzamora, R., Thali, R.F., Gong, F., Smolak, C., Li, H., Baty, C.J., Bertrand, C.A., Auchli, Y., Brunisholz, R.A., Neumann, D., Hallows, K.R., and Pastor-Soler, N.M. (2010). PKA Regulates Vacuolar H+-ATPase Localization and Activity via Direct Phosphorylation of the A Subunit in Kidney Cells. The Journal of Biological Chemistry 285, 24676–24685.

69. Eliasson, L., Ma, X., Renström, E., Barg, S., Berggren, P., Galvanovskis, J., Gromada, J., Jing, X., Lundquist, I., Salehi, A., Sewing, S., and Rorsman, P. (2003). SUR1 Regulates PKA-independent cAMP-induced Granule Priming in Mouse Pancreatic B-cells. The Journal of General Physiology 121, 181–197.

70. Dai, F.F., Bhattacharjee, A., Liu, Y., Batchuluun, B., Zhang, M., Wang, X.S., Huang, X., Luu, L., Zhu, D., Gaisano, H., and Wheeler, M.B. (2015). A Novel GLP1 Receptor Interacting Protein ATP6ap2 Regulates Insulin Secretion in Pancreatic Beta Cells. The Journal of Biological Chemistry 290, 25045–25061.

71. Baggio, L.L., and Drucker, D.J. (2007). Biology of Incretins: GLP-1 and GIP. Gastroenterology (New York, N.Y. 1943) 132, 2131–2157.

72. Campbell, J.E., Müller, T.D., Finan, B., DiMarchi, R.D., Tschöp, M.H., and D'Alessio, D.A. (2023). GIPR/GLP-1R dual agonist therapies for diabetes and weight loss—chemistry, physiology, and clinical applications. Cell Metabolism 35, 1519–1529.

73. Thomas, M.K., Nikooienejad, A., Bray, R., Cui, X., Wilson, J., Duffin, K., Milicevic, Z., Haupt, A., and Robins, D.A. (2021). Dual GIP and GLP-1 Receptor Agonist Tirzepatide Improves Beta-cell Function and Insulin Sensitivity in Type 2 Diabetes. The Journal of Clinical Endocrinology & Metabolism 106, 388–396.

74. Kapitza, C., Dahl, K., Jacobsen, J.B., Axelsen, M.B., and Flint, A. (2017). Effects of semaglutide on beta cell function and glycaemic control in participants with type 2 diabetes: a randomised, double-blind, placebo-controlled trial. Diabetologia 60, 1390–1399.

75. Kowluru, A. (2020). GPCRs, G Proteins, and Their Impact on β-cell Function. Comprehensive Physiology 10, 453–490.

76. Varney, M.J., Steyaert, W., Coucke, P.J., Delanghe, J.R., Uehling, D.E., Joseph, B., Marcellus, R., Al-awar, R., and Benovic, J.L. (2022). G protein–coupled receptor kinase 6 (GRK6) regulates insulin processing and secretion via effects on proinsulin conversion to insulin. The Journal of Biological Chemistry 298, 102421.

77. Iida, H., Kono, T., Lee, C., Krishnan, P., Arvin, M.C., Weaver, S.A., Jarvela, T.S., Branco, R.C.S., McLaughlin, M.R., Bone, R.N., et al. (2023). SERCA2 regulates proinsulin processing and processing enzyme maturation in pancreatic beta cells. Diabetologia 66, 2042–2061.

78. Chen, Y., Taylor, A.J., Fulcher, J.M., Swensen, A.C., Dai, X., Komba, M., Wrightson, K.L.C., Fok, K., Patterson, A.E., Klein Geltink, R.I., et al. (2023). Deletion of Carboxypeptidase E in β-Cells Disrupts Proinsulin Processing but Does Not Lead to Spontaneous Development of Diabetes in Mice. Diabetes (New York, N.Y.) 72, 1277–1288.

79. Meier, D.T., Rachid, L., Wiedemann, S.J., Traub, S., Trimigliozzi, K., Stawiski, M., Sauteur, L., Winter, D.V., Le Foll, C., Brégère, C., et al. (2022). Prohormone convertase 1/3 deficiency causes obesity due to impaired proinsulin processing. Nat Commun 13, 4761.

80. Avari, P., Eng, P.C., Hu, M., Chen, R., Popovic, N., Polychronakos, C., Spalding, D., Rutter, G.A., Oliver, N., and Wernig, F. (2023). A Novel Somatic Mutation Implicates ATP6V0D1 in Proinsulin Processing. Journal of the Endocrine Society 7, bvac196.

81. Hallakou-Bozec, S., Vial, G., Kergoat, M., Fouqueray, P., Bolze, S., Borel, A., Fontaine, E., and Moller, D.E. (2021). Mechanism of action of Imeglimin: A novel therapeutic agent for type 2 diabetes. Diabetes, Obesity and Metabolism 23, 664–673.

82. Anonymous Metformin restores prohormone processing enzymes and normalizes aberrations in secretion of proinsulin and insulin in palmitate-exposed human islets.

83. Wang, L., Liu, Y., Yang, J., Zhao, H., Ke, J., Tian, Q., Zhang, L., Wen, J., Wei, R., and Hong, T. (2014). GLP-1 Analog Liraglutide Enhances Proinsulin Processing in Pancreatic β-Cells via a PKA-Dependent Pathway. Endocrinology (Philadelphia) 155, 3817–3828.

84. Merglen, A., Theander, S., Rubi, B., Chaffard, G., Wollheim, C.B., and Maechler, P. (2004). Glucose Sensitivity and Metabolism-Secretion Coupling Studied during Two-Year Continuous Culture in INS-1E Insulinoma Cells. Endocrinology 145, 667–678.

85. Zhu, S., Larkin, D., Lu, S., Inouye, C., Haataja, L., Anjum, A., Kennedy, R., Castle, D., and Arvan, P. (2016). Monitoring C-Peptide Storage and Secretion in Islet β-Cells In Vitro and In Vivo. Diabetes (New York, N.Y.) 65, 699–709.

86. Schindelin, J., Arganda-Carreras, I., Frise, E., Kaynig, V., Longair, M., Pietzsch, T., Preibisch, S., Rueden, C., Saalfeld, S., Schmid, B., et al. (2012). Fiji: an open-source platform for biological-image analysis. Nat Methods 9, 676–682.

87. Kremer, J.R., Mastronarde, D.N., and McIntosh, J.R. (1996). Computer Visualization of Three-Dimensional Image Data Using IMOD. Journal of Structural Biology 116, 71–76.

88. Erozan, A., Lösel, P.D., Heuveline, V., and Weinhardt, V. (2024). Automated 3D cytoplasm segmentation in soft X-ray tomography. iScience 27, 109856.

89. Chen, J., Vanslembrouck, B., Loconte, V., Ekman, A., Cortese, M., Bartenschlager, R., McDermott, G., Larabell, C.A., Le Gros, M.A., and Weinhardt, V. (2022). A protocol for full-rotation soft X-ray tomography of single cells. STAR Protocols 3, 101176.

90. Smith, E., McDermott, G., Do, M., Leung, K., Panning, B., Le Gros, M., and Larabell, C. (2014). Quantitatively Imaging Chromosomes by Correlated Cryo-Fluorescence and Soft X-Ray Tomographies. Biophysical Journal 107, 1988–1996.

91. Haataja, L., Snapp, E., Wright, J., Liu, M., Hardy, A.B., Wheeler, M.B., Markwardt, M.L., Rizzo, M.A., and Arvan, P. (2013). Proinsulin Intermolecular Interactions during Secretory Trafficking in Pancreatic β Cells. The Journal of Biological Chemistry *288,* 1896–1906.

EXPERIMENTAL MODEL AND STUDY PARTICIPANT DETAILS

Cell Culture

Rat insulinoma INS-1E cells were obtained from Pierre Maechler's lab (University of Geneva)[84] and cultured at 37°C with 5% CO_2. The cells were maintained in Optimized RPMI 1640 media, supplemented with 10 % fetal bovine serum (FBS), 0.05 mM β-Mercaptoethanol, and 1x Penicillin-Streptomycin. Cells were seeded at a 4.0×10^4 cells/cm² density in T75 flasks and passaged according to previously documented protocols[31]. Quality control was conducted by testing the insulin response using an ELISA assay (see below) in response to increasing glucose concentrations.

Animal Model

For experiments involving primary β-cells, animal procedures were approved and conducted per the Institutional Animal Care and Use Committee (IACUC) guidelines at the University of Southern California (Animal Use Protocol #21120). The C57BL6/J mouse model expressing human proinsulin tagged with C-peptide-Superfolder Green Fluorescent Protein (CpepSfGFP) was provided by Peter Arvan (University of Michigan).[85] Experiments were performed on mice around 2 - 3 months of age.

METHOD DETAILS

Primary β-cell isolation

Islets from the mice were isolated and dissociated according to previously published protocols (4). Briefly, the mouse pancreas was perfused and digested at 37°C using a liberase and DNAse enzyme blend. Islets were handpicked manually and incubated overnight in RPMI 1640 media at 37 °C. Islets were dissociated at 37°C using Accumax Cell Dissociation Solution and subsequently processed for SXT sample preparation.

Insulin and Proinsulin quantifications using ELISA

Insulin and proinsulin quantification assays were performed following previously established protocols.[18] Four days prior to the assay, INS-1E cells were plated in 96-well plates at a density of 4.0×10^4 cells per well. The cells were washed with 1 x PBS and then starved in Krebs-Ringer Bicarbonate buffer (KRBH) (115 mM NaCl, 24 mM $NaHCO_3$, 5 mM KCl, 1 mM $MgCl_2$, and 1 mM $CaCl_2$) supplemented with 0.2 % bovine serum albumin (BSA) ,10 mM HEPES, and 1.1 mM glucose buffer, maintained at a pH of 7.4 at 37°C for 30 minutes before stimulation. For the unstimulated cells, the starvation condition was the only treatment performed. After starvation the cells were incubated at 37°C with either glucose-only (25 mM) or glucose in conjunction with the various insulinotropic stimuli (Glimepiride: 100 nM, GKA-50: 100 nM, TAK-875: 10 µM, GIP: 10 nM, and Ex-4: 10 nM) for 30 minutes. After stimulation, the supernatants were collected, centrifuged at 4°C for 10 minutes to pellet any detached cells, and stored at -80°C until further analysis. Following stimulation, cells were lysed on ice for 30 minutes in a custom lysis buffer (0.05 % Tween 20 along with 0.5 % Triton X-100 in 1 x PBS) supplemented with protease inhibitors. The lysates were collected and centrifuged and stored at -80C until further analysis. The supernatant was diluted 5x and the lysate was diluted 256x and the insulin and proinsulin levels were quantified using commercially available ELISA kits (Rat Insulin and Proinsulin for INS1E; Mouse Insulin and Proinsulin for islets). The assays were performed according to the manufacturer's instructions. The secreted and intracellular insulin/proinsulin ratios were calculated by dividing the values obtained from the supernatant and cell lysates, respectively.

SXT sample preparation

For SXT data collection, INS-1E cells were stimulated in a manner similar to that used in the ELISA assays. Cells were first collected from T75 flasks and then transferred to suspension culture in Eppendorf tubes. After this, the cells were immediately starved in KRBH buffer at 37°C for 30 minutes, followed by stimulation with the insulinotropic stimuli for 30 minutes at 37°C with 5 % CO_2. After stimulation, cells were collected, centrifuged and resuspended in 1 x PBS and kept on ice. The single cells were then subsequently loaded into custom glass capillaries with diameters ranging from 6–10 µm according to previously established protocols.[89] For primary cell stimulation, whole islets were stimulated with glucose

842   (16.7 mM) and Ex-4 (10 nM), after which they were dissociated into single cells. The unstimulated islets
843   were processed fresh from the basal media (11.1 mM Glucose). After dissociation, single cells were then
844   collected, resuspended in 1xPBS, kept on ice and subsequently loaded. The capillaries were cryo-fixed
845   by plunge-freezing the capillary into liquid ethane cooled by liquid nitrogen to preserve cellular structure
846   for subsequent X-ray tomography analysis.

SXT data collection

848   SXT was performed using the XM-2 at the National Center for X-Ray Tomography, located at Lawrence
849   Berkeley National Laboratory. X-ray projection images were collected at an energy of 517 eV using a 50
850   nm resolution objective lens. To minimize radiation damage, samples were maintained under a steady
851   stream of liquid nitrogen-cooled helium gas. Projection images were sequentially captured at 2°
852   increments around a 180° axis of rotation (capillary axis), with an exposure time of 350 ms. Tomograms
853   were reconstructed from the acquired projections using AREC3D, with pixel intensity normalized to
854   attribute accurate linear absorption coefficient (LAC) values across all samples.[37] To correlate SXT data
855   with the corresponding fluorescent signal (to identify hProCpep-sfGFP positive β-cells), the position of
856   each cell was marked for each capillary and manually retrieved later during image post-processing.

Tomogram segmentation

858   Segmentation of cellular structures was performed using Amira 2021.2 - 2023.1. software. Organelles
859   were identified based on prior reports.[18,20,21] Briefly, mitochondria were identified based on their cylindrical
860   morphology and characteristic LAC. The cell membrane and nuclear membrane were identified based on
861   local LAC contrast with the exterior of the cell and the cytosol respectively. Nuclear euchromatin and
862   heterochromatin was observed and segmented but not included in this report. Lipid droplets were
863   identified by the large morphology (greater than 600nm) and a mean LAC greater than 0.55 μm^{-1}, in
864   accordance with several reports. ISGs were identified based on their shape, size, characteristic LAC and
865   local LAC contrast. Although ISGs resemble lipid droplets in shape, they have significantly smaller
866   diameters and lower mean LAC values. The differences in LAC values between ISGs and Lipid droplets
867   are easily distinguishable for each cell during segmentation. The plasma membrane was initially
868   segmented using the ACSeg 3D UNET model on Biomedisa[88], followed by manual refinement using the
869   "paintbrush" tool in Amira. The nucleus was segmented semi-automatically using the "paintbrush" and
870   "interpolation" tools. Mitochondria and ISGs were segmented using a combination of the "magic wand"
871   tool and manual segmentation.

Organelle quantification

873   Mean organelle volume, number and LAC values were obtained using Amira. The mean LAC values were
874   acquired by calculating the mean LAC for the organelle label field similar to our previous reports (5, 8).
875   Future work will focus on analyzing individual mitochondria for a more in-depth analysis similar to the
876   ISGs

ISG quantification

878   Mean ISG label field LAC was calculated using Amira by pooling voxels from the entire insulin label field
879   and obtaining the mean value. To assess statistics on individual ISG parameters, the ISG segmentation
880   mask was thresholded, separated into distinct ISGs and then analyzed using Amira. Mean ISG LAC was
881   gathered by calculating the mean LAC for each ISG and then computing the mean of all the ISGs present
882   in a condition. The parameters extracted for individual ISGs using the "label analysis" tool on Amira were:
883   Minimum LAC, 25th percentile LAC, median LAC, mean LAC, 75th percentile LAC, maximum LAC,
884   diameter, volume, surface area, skew, kurtosis and standard deviation. To assess the distribution of these
885   parameters across spatial zones, the cell mask was thresholded out and a "distance map" was created
886   using the Euclidean distance transform parameters. This EDT map for each cell was then overlayed on
887   the ISG label field and the average position of each ISG in the EDT map computed. The distances were
888   normalized across cell by accounting for the maximum EDT in each cell and dividing that value to the

889 individual EDT obtained for the ISGs for that respective cell. ISG Biomaterial Amount Index (BAI) was
890 defined as:

891

$$ISG\ BAI = \frac{V_{ISG} \times LAC_{ISG}{}^3}{100000}$$

892

893 Where V_{ISG} is the Volume of the ISG (μm^3) and LAC_{ISG} is the mean LAC (μm^{-1}) for the same ISG. The BAI
894 is a dimensionless variable that combines volumetric and densitometric properties. A higher BAI would
895 suggest more biomaterial packed in an ISG.

Visualization and 3D rendering

897 3D rendering of the segmented organelle masks was done using Blender. Blender renderings were
898 modified to appropriately shade different ISGs based on the mean ISG LAC.

Cryo-fluorescence microscopy

900 Cryogenic fluorescence data of the cells, along with their corresponding bright field images, were
901 acquired using a custom-built cryogenic fluorescence microscope equipped with a commercial dual
902 spinning disk head.[90] A 491 nm laser was used to detect the C-peptide-SfGFP fluorescent signal. To
903 identify primary β-cells, we correlated the fluorescence signal with the X-ray absorption signal collected
904 from the same specimen. For imaging lysosomes, a 561 nm laser was used. Maximum intensity
905 projections were used to for both, brightfield and fluorescence images.

Structured Illumination Microscopy (SIM) imaging

907 For imaging lysosomes, GRINCH cells (expressing hPro-CpepSfGFP) were grown on 8-well covered
908 chamber slips 48-hours prior to imaging. GRINCH cells were cultured similar to INS-1E cells as
909 mentioned earlier.[91] The cells were stained with Lysotracker Red and incubated at 37°C and 5% CO_2 for
910 5 minutes. Structured illumination (SI) microscopy was carried out using the DeltaVision OMX Microscope
911 equipped with a 60□x□1.42, PlanApo N, Oil Immersion objective. The 488nm and 568nm laser lines
912 were used to image the ISGs and Lysosomes respectively. Images were captured in the SI mode with a
913 Z-spacing of 125 nm and reconstructed using SoftWorx software.

Confocal fluorescence imaging

915 For imaging lipid droplets (LDs), INS-1E cells were grown on 8-well covered chamber slips 72-hours prior
916 to imaging. For the unstimulated condition, cells were starved with KRBH buffer for 25 minutes, followed
917 by 5 minutes of starvation in KRBH buffer containing BODIPY 493/503. For the TAK-875 condition, cells
918 were first starved for 30 minutes in KRBH buffer and then treated with 25mM glucose and 10μm of TAK-
919 875 for 25 minutes after which the cells were treated for 5 minutes with the same stimulation solution in
920 conjunction with BODIPY 493/503. All incubations were performed at 37°C and 5% CO_2. After LD
921 staining, cells were washed with 1xPBS after which the cells imaged using the Leica MICA confocal
922 microscope equipped with a high contrast plan apochromatic (HC PL APO) CS2 63x/1.20 water
923 immersion lens. The fluorescence image was processed using LASX software (Leica Application Suite X)
924 with the Lightning deconvolution. The number of lipid droplets were calculated using Imaris using the cell
925 generation pipeline. The image z-stacks were then transferred to ImageJ where maximum intensity
926 projections were created.

QUANTIFICATION AND STATISTICAL ANALYSIS

928 All quantitative data were graphed and analyzed using GraphPad Prism 10.1.2 software. Statistical
929 analysis was performed within Prism and are mentioned in the figure legends along with sample size for

930   each analysis. Statistical significance was set at $*P < 0.05$; $**P < 0.01$; $***P < 0.001$; $****P < 0.0001$ for all
931   analyses.